Chapter 4

Recovery of CuO nanoparticles from WPCBs of obsolete computer motherboards

4. Recovery of CuO nanoparticles from WPCBs of obsolete computer motherboards

4.1. Introduction

Oxides of transition metals, such as CuO, ZnO, NiO exhibit typical photocatalytic and catalytic attributes (Meshram et al., 2012). Monoclinic cupric oxide, Cu(II)O, a p-type semiconductor, has a bandgap range of 1.2-1.8 eV (Radhakrishnan and Beena, 2014). CuO offers diverse potential applications in fields of catalysis (Juan Wang et al., 2016) due to its thermal stability, superconductivity, photocatalytic behaviour (Quirino et al., 2018).

Many strategies such as precipitation method (Shahmiri et al., 2012), sol-gel method (Aparna et al., 2013), solvothermal process (Saghatforoush et al., 2011), hydrothermal process (Liu et al., 2019), electrochemical discharge method (Singh et al., 2017), sonochemical method (Singh et al., 2017), spray pyrolysis (Singh et al., 2017), microwave irradiation (Liang and Zhu, 2004), micro-emulsion (Dodoo-Arhin et al., 2012) etc. have been employed for synthesis of CuO nanostructures. Among these methods, precipitation method is a cost-efficient approach for better yield and mass production.

Copper forms a major part of the metallic fraction in the PCBs. The quintessential concentration of copper (60 kg/t-270 kg/t) is higher than its corresponding ores (Panda et al., 2021). Therefore environmentally safe recycling practices for copper reclamation from WPCBs can help in up keeping natural resources (Kaya, 2016) and a step towards sustainable development of resources. There are many research articles reporting the formation of copper-based products from electronic scrape. Xiu and Zhang reported the synthesis of Cu_2O nanoparticles with 5-40 nm size by combination of supercritical water and electrokinetic process (Xiu and Zhang, 2012). Ultrafine zero-valent copper and Cu_2O nanoparticles were prepared by supercritical methanol method from nitric acid pre-treated

WPCBs (Xiu et al., 2017). Panda et al. recovered copper as CuO NPs by roasting of PCBs in ammonium chloride followed by precipitation with ammonia solution (Panda et al., 2021). Yi and Chandren synthesized CuO NPs from waste SIM cards by sodium hydroxide precipitation at 100ºC, followed by calcination, and utilized them for phenol degradation (Yi and Chandren, 2022). Ravi et al. developed CuO NPs from WPCBs via a green synthesis route with the involvement of *Catharanthus roseus* plant extract as a reducing agent (Ravi et al., 2023). However, a study on direct recovery of CuO nanoparticles from delaminated PCBs by facile precipitation route has not been reported in already published literatures.

In the present study, the production of copper oxide nanoparticles from discarded PCBs of computer motherboards is investigated. Nickel and zinc concentration is lower in PCBs of computer motherboards than in PCBs of mobile phones, printers, internet routers, hard disk drive, random access memory, and lithium ion batteries (Gautam et al., 2022). So contamination of CuO NPs by co-precipitation of nickel and zinc along with copper can be avoided. PCB is composed of glass fiber reinforced polymer epoxy resin with embedded Cu sheet, consequently which may change to glassy slag on thermal heating and restrain the diffusion of solvent (leachant) and dissolution of the metal. Heating the PCB pieces below 130.12°C (the glass transition temperature T_g), leaves it frozen leading to low Cu recovery due to minimal Cu and solvent interaction. Separating metallic and nonmetallic fraction exposes metallic fraction and facilitates better solvent interactions leading to better Cu recovery (Wath et al., 2016). Also, Copper is closely attached to plastic matrix due to the structure of copper clad laminate of PCBs, and thus it is necessary to liberate Cu. Generally, pre-concentration is conducted before copper leaching to reduce the treatment burden of leaching process (Wang et al., 2021). Hence, liberation of Cu-foils at the

beginning and synthesis of CuO-NPs from the recovered foils can be a promising way to increase the yield and purity of the synthesized nano- product. Since the non-metallic components of WPCBs are separated after dissolution in organic solvent, most of the non-metallic components do not end up in the residue post leaching. So this counters the difficulty of residue disposal. No chemical precursor is used here as initial starting material for copper source. Besides, no chemical surfactant, particle size stabilizer, substrate or template is used for nanoparticle synthesis. So this is a facile route of synthesis of CuO NPs from e-waste where copper-rich precursor is prepared from the PCB leached solution and sodium hydroxide is used as precipitant.

4.2. Synthesis of CuO NPs from Cu-rich leach liquor

Metal clads recovered from the pre-processing step of discarded printed circuit boards of obsolete computer motherboards are subjected to nitric acid leaching under optimized leaching parameters. The parameters of leaching were 3 M HNO_3, 30ºC temperature, 2 h time period, 50 g/L pulp density and 500 rpm stirring speed. After filtration of leaching solution, the blue-coloured filtrate was magnetically stirred for 20 min at pre-set temperature (30 or 60ºC). Alkali solution (1 M, 2 M NaOH; 1 M, 2 M ammonia solution) was added dropwise to the leached solution till pH of the solution reached 8.5. Curdy blue precipitates were formed. The precipitates were harvested by centrifugation and washed several times to get rid of any impurity and dried in vacuum oven at 60°C overnight. After harvesting the precipitates by centrifugation, the alkali solution can be further added to the supernatant solution to see if any zinc is recovered as zinc hydroxide in the pH range of zinc hydroxide precipitation. The supernatant solution is treated before disposal to prevent any secondary pollution. Obtained dry powder was ground with mortar pestle and calcined at 400°C for 4 h in muffle furnace. After calcination black powder was collected, and

subjected to various characterization methods such as XRD, FTIR, SEM-EDX, TEM, UV-visible spectroscopy, XPS, and surface area analysis. In this way four samples were prepared as given in *Table 4.1*. This recovery route is economical, eco-friendly and can be scaled up for production of nanomaterials at relatively low temperature.

Table 4.1 List of different samples obtained from the synthesis route

Alkali solution	Pre-set temperature of mixing of alkali and leached solution (ºC)	Whether precipitation is observed, or not	Sample nomenclature
1 M NaOH	30	Yes	N1
1 M NaOH	60	Yes	N2
2 M NaOH	30	Yes	N3
1 M ammonia	30	No	-
1 M ammonia	60	No	-
2 M ammonia	60	Yes	N4

Since NaOH is a strong base and ammonia is a weak base, so NaOH appears to be a better reagent than ammonia for precipitation. As the concentration of NaOH was increased from 1 to 2 M, precipitation was observed to take place at a faster rate. Later it was observed that the crystallite size, particle size and morphology of the obtained nanoproduct also changed as the concentration of precipitant was increased. The reduction of Gibb's free energy (*Eq. (4.1)*) is the driving force for both nucleation and growth.

$$\Delta G = (-KT/\Omega)\, ln\,(C/C_0) \qquad (4.1)$$

where C is the concentration of the solute C_0 is the equilibrium concentration or solubility, Ω is the atomic volume. From above equation we can see that as the concentration increases Gibb's free energy increases. To lower this energy the particles continue to grow unless the minimum energy required for stability is achieved. The hydroxyl ion concentration plays

an important role for the morphology and size. After nucleation the hydroxyl ions excess in solution is adsorbed on the polar faces of growing particle i.e. it takes nano rod shape. For even higher concentration hydrolysis/condensation is uncontrolled then no preferential growth is observed along c axis and so the particles appear in quasi spherical shape. The critical size represents the limit how small nanoparticles can be synthesized. Critical size (*Eq. (4.2)*) and critical energy (*Eq. (4.3)*) is given by

$$r^* = \frac{-2\gamma}{\Delta G_v} \quad (4.2)$$

and

$$\Delta G^* = \frac{16\pi\gamma}{3(\Delta G_v)^2} \quad (4.3)$$

where γ is the surface energy per unit area and ΔG_v change of Gibb's free energy or volume energy.

To reduce the critical size and free energy one need to increase the change of Gibb's free energy, ΔG_v and reduce the surface energy of the new phase. Hence the particle size increased with increase in base concentration (Jyoti et al., 2013; Moazzen et al., 2013).

When base is added, first it hydrolyzes to produce the OH^- and Na^+ or ammonia. Then, the OH− forms a complex with Cu^{2+}, followed by thermal decomposition into CuO. When the pH was increased by adding $NH_3{\cdot}H_2O$, the ammonia hydrolyzed into NH_4^+ and hydroxide giving rise at the same way to the increases of OH^- concentration in the solution (Amin et al., 2011). The following chemical reactions are governing the growth process:

$NaOH \leftrightarrow Na^+ + OH^-$

$NH_3 \cdot H_2O \leftrightarrow NH_4^+ + OH^-$

$Cu^{2+} + 2OH^- \leftrightarrow Cu(OH)_2$

$Cu(OH)_2 \leftrightarrow CuO + H_2O$

$Cu(OH)_2 + OH^- \leftrightarrow [Cu(OH)_4]^{2-}$

4.3. Characterization of the recovered products

4.3.1. Structural properties analysis (XRD, FTIR, SEM-EDS)

The XRD pattern presented in *Figure 4.1* allowed the determination of the structure and phase composition of the particles produced using NaOH and $(NH_4)OH$ solution. The presence of Bragg reflections at 2θ values of 41.351 and 45.174º indicates the crystallographic planes (002) and (111) of monoclinic CuO (JCPDS card no. 89-5899). In sample N1 and N2 all reflection peaks matched with the d-spacing of CuO. In sample N3 and N4, apart from CuO reflections, very low intensity peaks of ZnO are also observed which matched with JCPDS card no. 79-0206. The distinct and well-defined peaks in the XRD pattern provide further confirmation of the product's high crystallinity. Importantly, no side peaks corresponding to any by-products like $Cu(NO_3)_2$, $Cu(OH)_2$, Cu_2O or Cu were observed in the recorded pattern, which validated the formation of metal oxides. There is no nickel-based compound in the prepared samples as the synthesis conditions were not favourable for the formation of NiO or other hydroxides. Nickel precipitates as hydroxide at pH 10.0-10.5 (Zainuddin et al., 2019). But the pH involved in the synthesis step was around 8.5. The average crystallite size is found from Debye-Scherrer's formula (*Eq. (4.4)*),

$$Crystallite\ size\ D = \frac{0.9\lambda}{\beta.cos\theta} \quad (4.4)$$

where D is average crystallite size, λ is x-ray wavelength (here, 1.789 Å), β is Full Width at Half Maximum (FWHM) of each peak (in radians), and θ is Bragg diffraction angle (in

radians) (Parekh et al., 2021). The slightly increasing average crystallite size values as obtained are enlisted in *Table 4.2*.

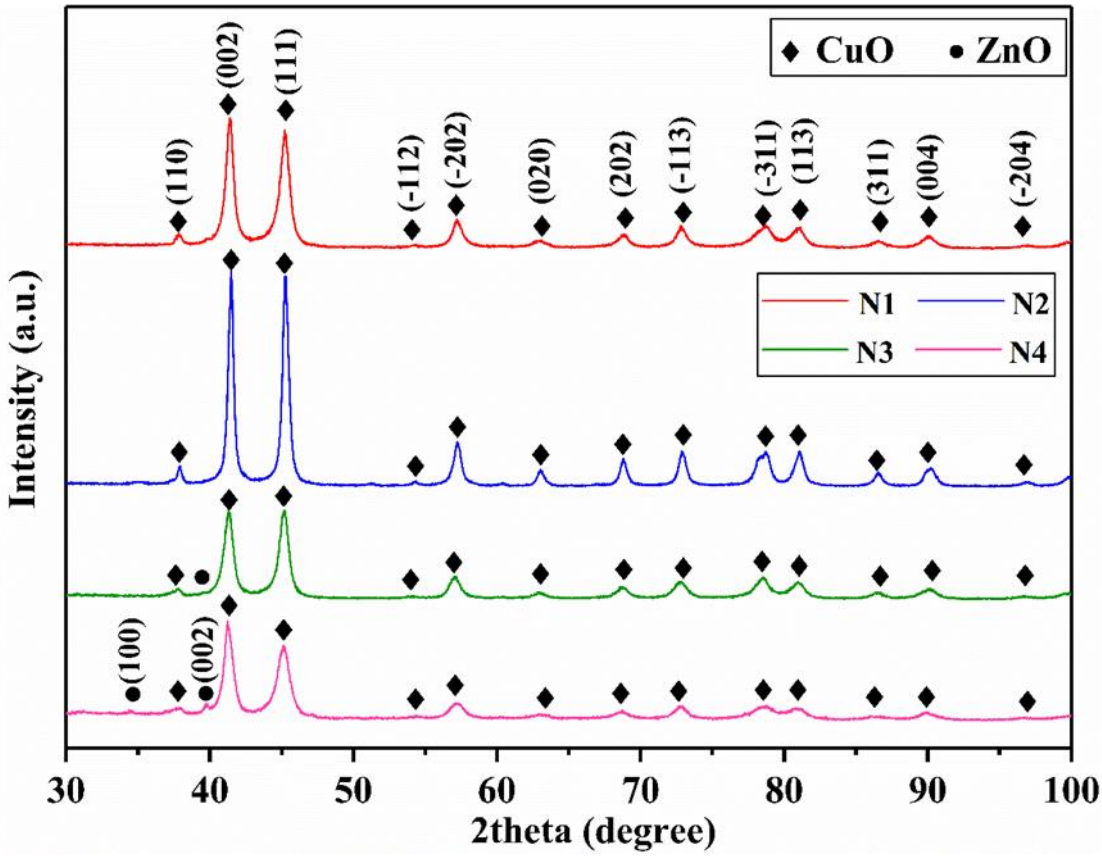

Figure 4.1 X-ray diffraction pattern of calcined N1, N2, N3, and N4 samples

Table 4.2 Average crystallite size of as-synthesized N1, N2, N3, and N4 samples

Sample name	N1	N2	N3	N4
Average crystallite size (nm)	18.049	19.236	20.742	21.572

Figure 4.2 displays the FTIR spectra of N1, N2, N3, and N4 samples, which were measured using infrared spectroscopy. This analytical technique offers enhanced structural insights by examining the presence or absence of distinct absorption bands, aiding in the identification of key functional groups within the compounds. In the spectra, distinct bands

were observed between 620-420 cm^{-1} wavenumber, which are assigned to Cu-O stretching vibrations, confirming the formation of monoclinic CuO. This is consistent with previous reports (El-Atawy et al., 2022; Keabadile et al., 2020; Mageshwari and Sathyamoorthy, 2013). The absorption peaks detected at 1630 and 3440 cm^{-1} can be attributed to the bonding of H-O-H and stretching of O-H bonds. These vibrations occur due to the presence of water molecules adsorbed on the Cu-O surface (Fatoni et al., 2021; Kayani et al., 2015; Rajkumar et al., 2020; Tanvir et al., 2016). Further heating can eliminate these adsorbed water molecules (Arun et al., 2015). The absence of any peaks corresponding to impurities such as CH_2, CH_3, or other polymers in the FTIR spectrum confirms the formation of pure metal oxide. This observation aligns well with the XRD analysis, leading us to conclude that the obtained product is indeed CuO.

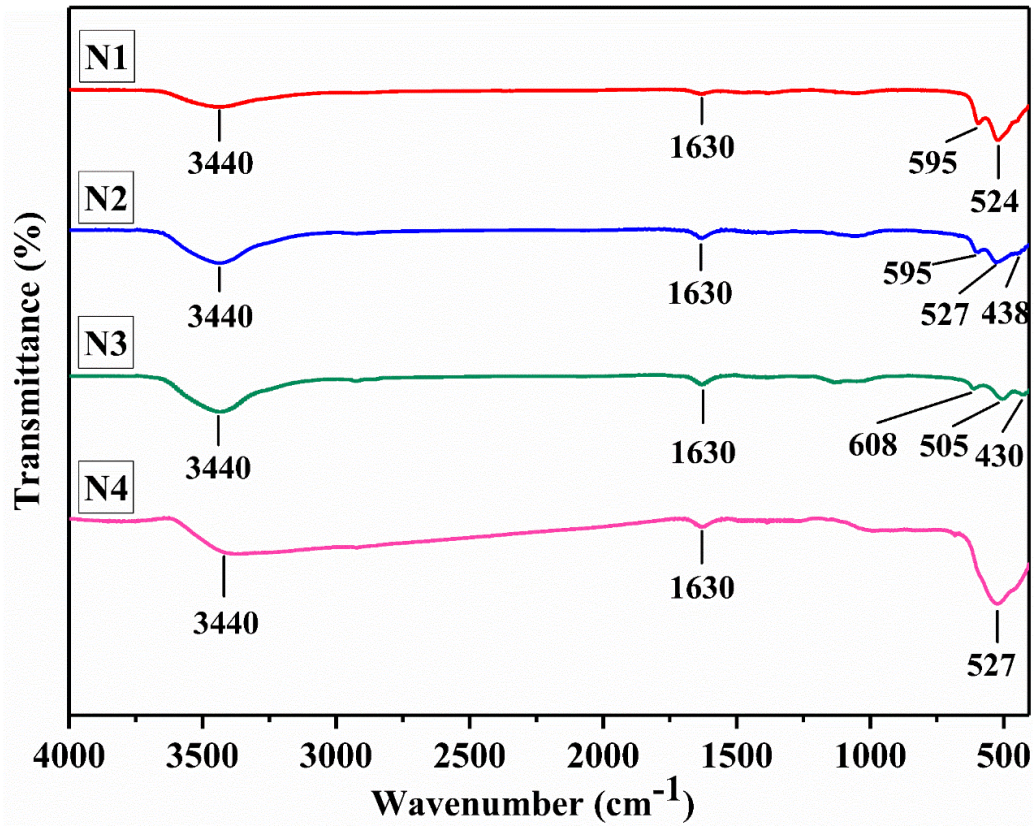

Figure 4.2 FTIR spectra of calcined N1, N2, N3, and N4 powders

SEM-EDX analysis was done to reveal the surface morphology of the prepared samples. For N1 and N2 (*Figure 4.3(a,c)*), it shows a homogenous distribution of irregular spherical morphology. EDX spectrum of N1 and N2 (*Figure 4.3(b,d)*) clearly confirmed the presence of [Cu] and [O] peaks, thus confirming the formation of CuO. The carbon peak is ascribed to the double tape used for mounting the powder sample during EDX analysis (Mbenga et al., 2022). N3 sample shows sheet-like morphology (*Figure 4.3(e)*). N4 shows sheets rearranged to form large sphere-like morphology (*Figure 4.3(g)*). In the EDX of N4 (*Figure 4.3(h)*), peak of [Zn] is observed along with [Cu] and oxygen [O], confirming the presence of ZnO along with CuO, which is in agreement with the XRD data of N4 sample.

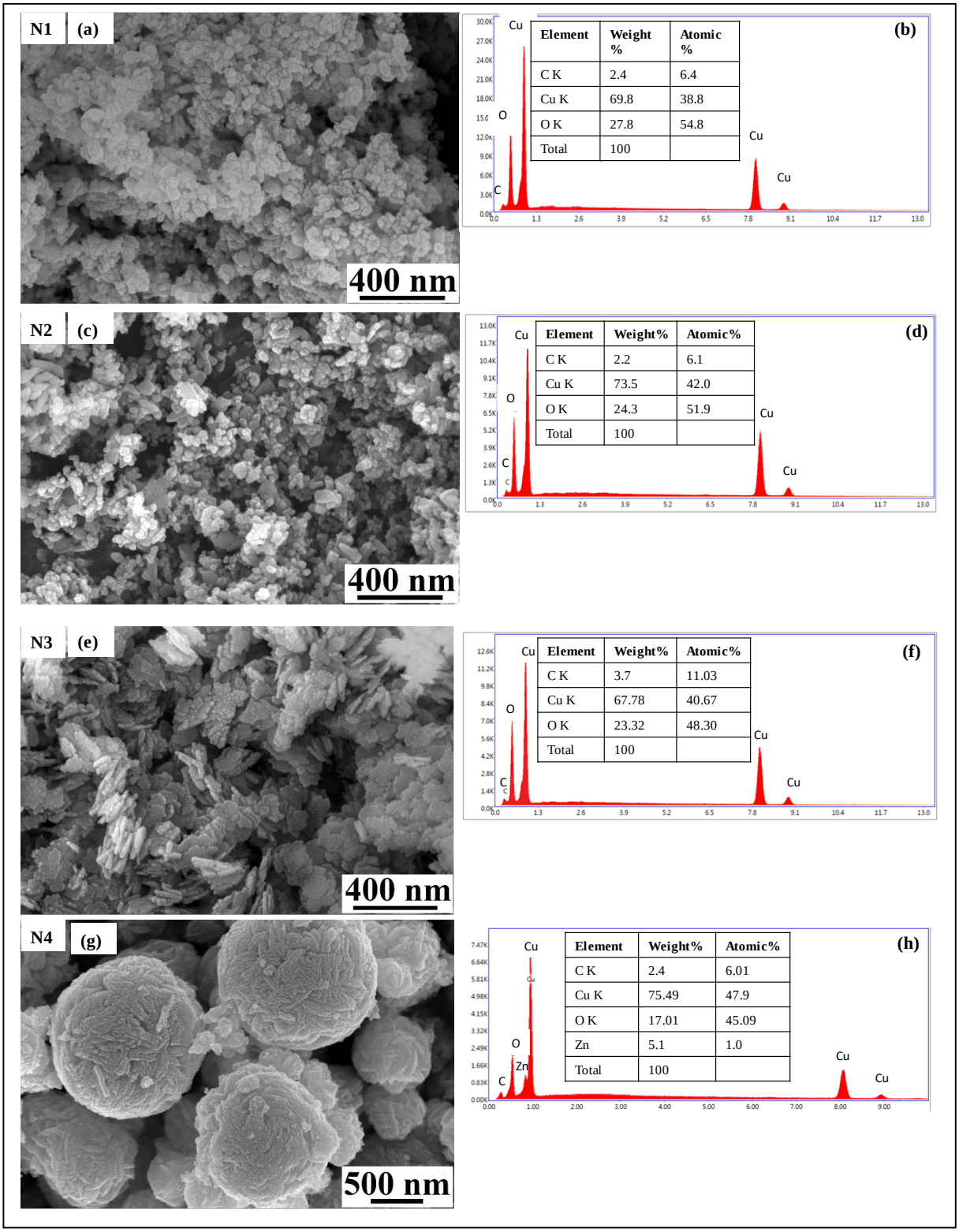

Figure 4.3 SEM-EDX analysis of N1 (a,b), N2 (c,d), N3 (e,f), and N4 (g, h)

4.3.2. Optical bandgap energy analysis

The UV-visible solid state study was performed to determine the optical bandgap energy of CuO NPs using Tauc's formula (Krishnan et al., 2021) (*Eq. (4.5)*),

$$(\alpha h\nu)^n = A(h\nu - E_g) \quad (4.5)$$

where α is the molar absorptivity coefficient, h is Planck's constant, ν denotes frequency, A is material constant, E_g denotes bandgap energy, n is type of transition value which is equal to 2 or 1/2 for a direct or indirect transition semiconductor respectively (Abaker et al., 2011). The E_g for the direct transition is assessed from the intercept of the extrapolation of the straight line drawn on the linear portion of the $(\alpha h\nu)^2$ versus hν plot on the x-axis at α=0. The direct band gap in *Figure 4.4* is determined to be 1.93, 1.97, 1.86, and 1.48 eV for N1, N2, N3, and N4 samples which is more than that reported for bulk CuO (1.8 eV) (Radhakrishnan and Beena, 2014; Santra et al., 1992), indicating a blue shift in the values (Rehman et al., 2011). This increase in the band gap of CuO nanoparticles is typical of quantum confinement effects happening due to the occurence of nano-sized particles (Liu et al., 2006). Rehman et al. have reported in their study that direct band transition energies decrease with increasing particle size (Rehman et al., 2011).

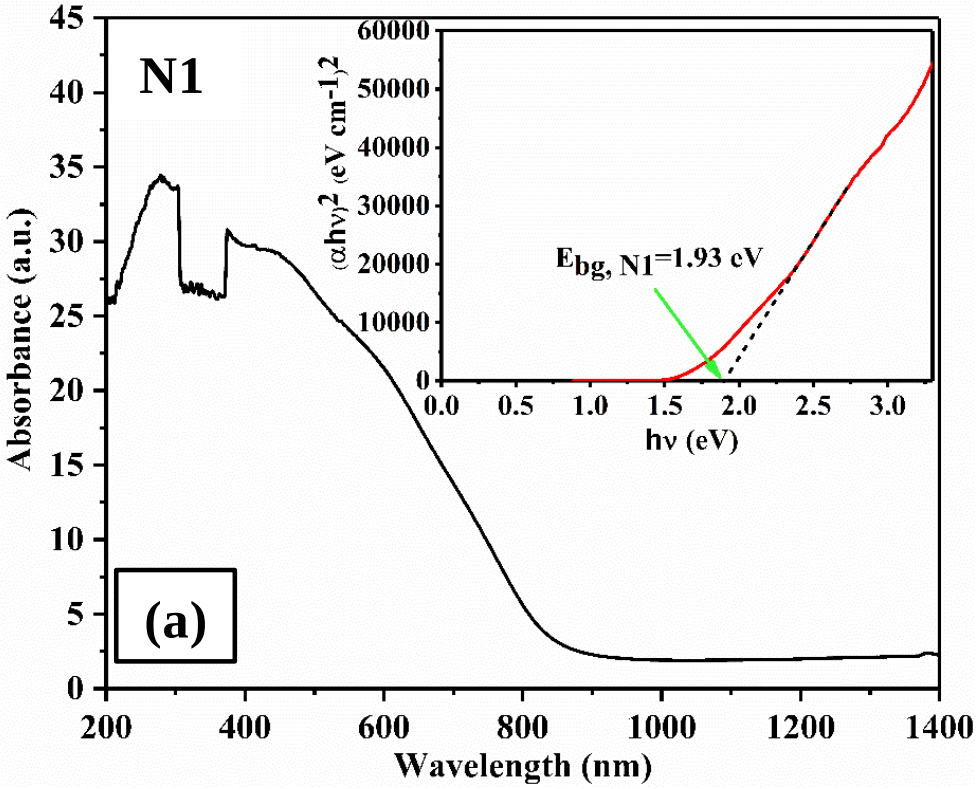
N1
(a)
Absorbance (a.u.)
Wavelength (nm)
(αhν)2 (eV cm-1)2
hν (eV)
Ebg, N1=1.93 eV

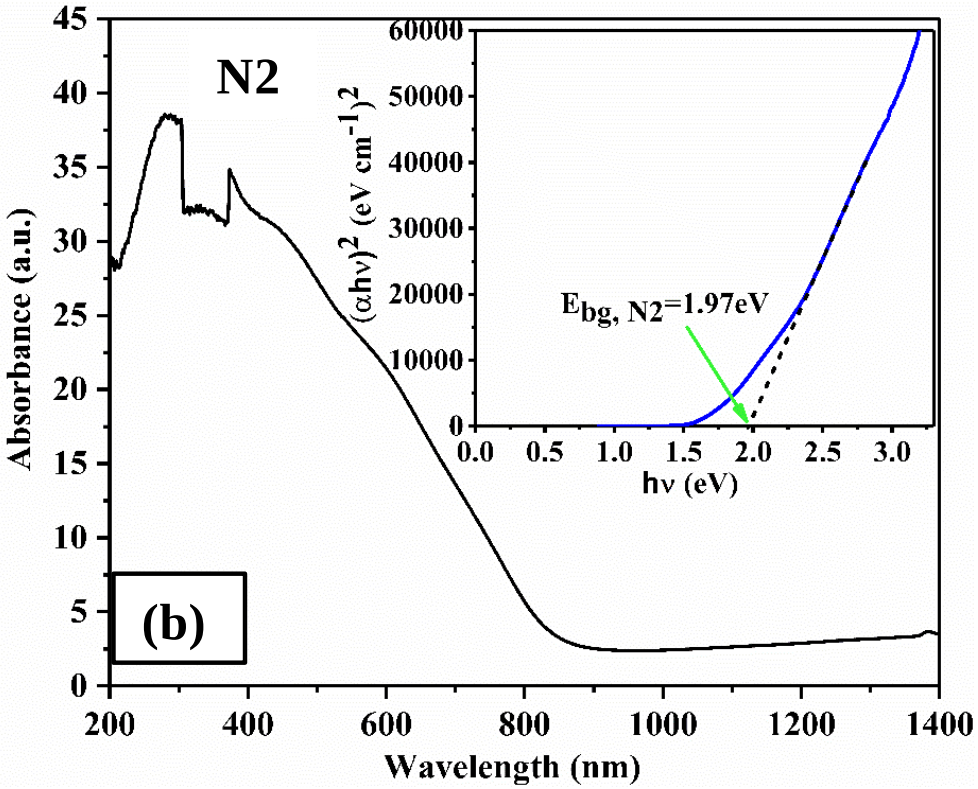
N2
(b)
Absorbance (a.u.)
Wavelength (nm)
(αhν)2 (eV cm-1)2
hν (eV)
Ebg, N2=1.97eV

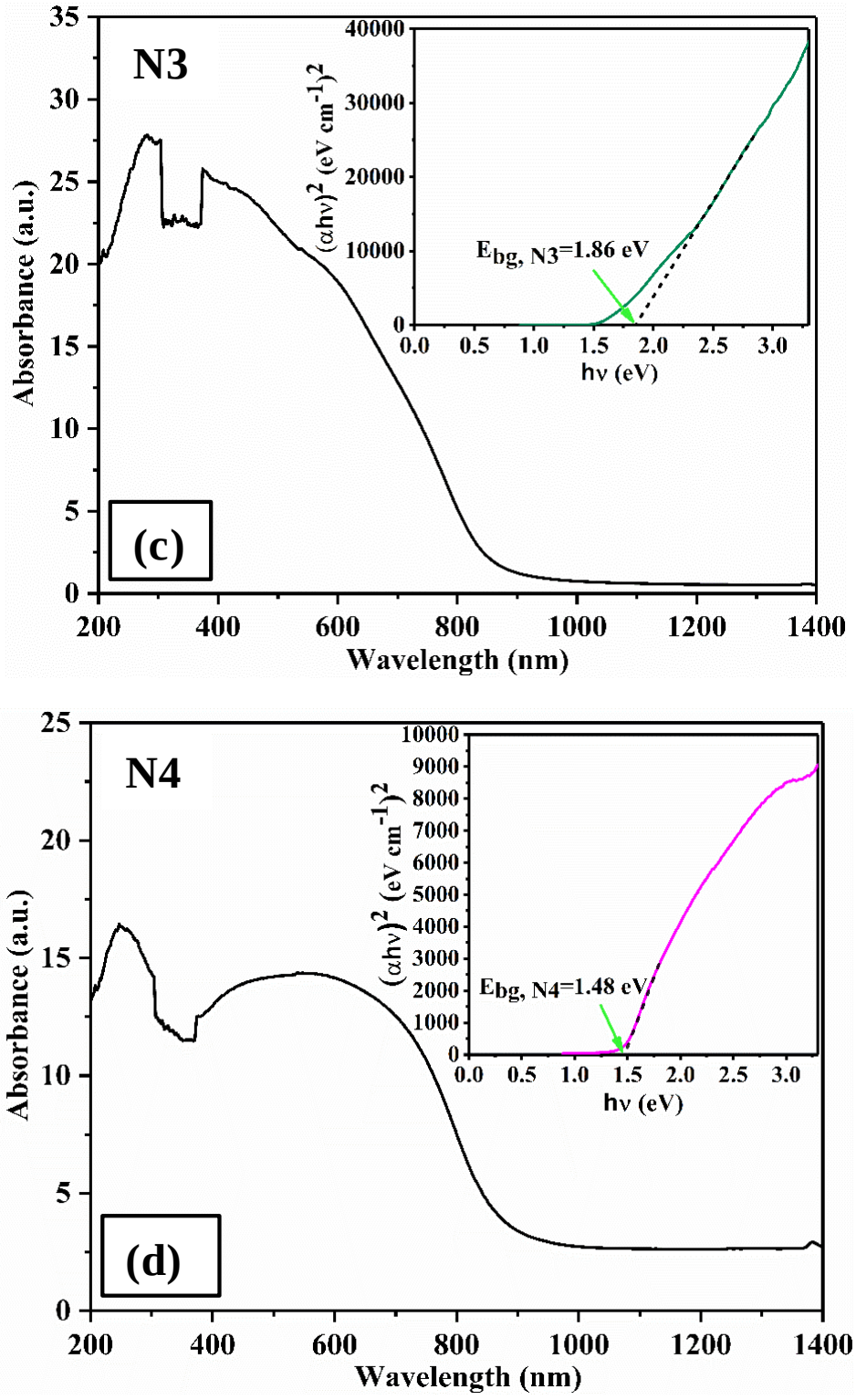

Figure 4.4 UV-vis diffuse reflectance spectrum and the energy band gap (inset) of (a) N1, (b) N2, (c) N3, and (d) N4 samples

4.3.3. TEM micrograph analysis

TEM is used to reveal the shape, size, and structure of the samples. TEM reveals that N1 has spherical morphology (*Figure 4.5(a,b)*). The nanostructures are made of assorted sizes of CuO NPs. TEM images also confirmed the connectivity between the spheres (*Figure 4.5(b)*) which was also seen in SEM images. The Selected Area Electron Diffraction (SAED) pattern (*Figure 4.5(c)*) shows discrete spots with electron rings, which are characteristic of polycrystalline nature of CuO. The SAED pattern shows various diffraction rings of monoclinic CuO and very well agree with the XRD analysis. 10 nm resolution studies of synthesized N1 NPs (*Figure 4.5(d)*) shows 0.15 nm d-spacing, corresponding to the distance of [-113] plane of monoclinic CuO. From the particle size distribution curve of N1 (*Figure 4.5(e)*), the mean particle size was found to be 18.709±5.662 nm.

Similarly, for N2, spherical morphology is observed (*Figure 4.6(a,b)*). The interplanar d-spacing (*Figure 4.6(d,e)*) shows 0.27 and 0.141 nm d-spacing corresponding to the distance of [110] and [-311] plane of the monoclinic CuO. From the particle size distribution curve (*Figure 4.6(f)*), the average particle size is found to be 19.973±6.036 nm.

N3 shows sheet-like morphology with mean particle size of 55.997±16.892 nm (*Figure 4.7(a-c,f)*). The SAED pattern (*Figure 4.7(d)*) shows various diffraction rings of monoclinic CuO. The interplanar d-spacing (*Figure 4.7(e)*) shows 0.186 nm distance corresponding to [-202] plane of monoclinic CuO. N4 shows spherical morphology (*Figure 4.8*) with mean particle size of 975±304 nm which are termed as microspheres.

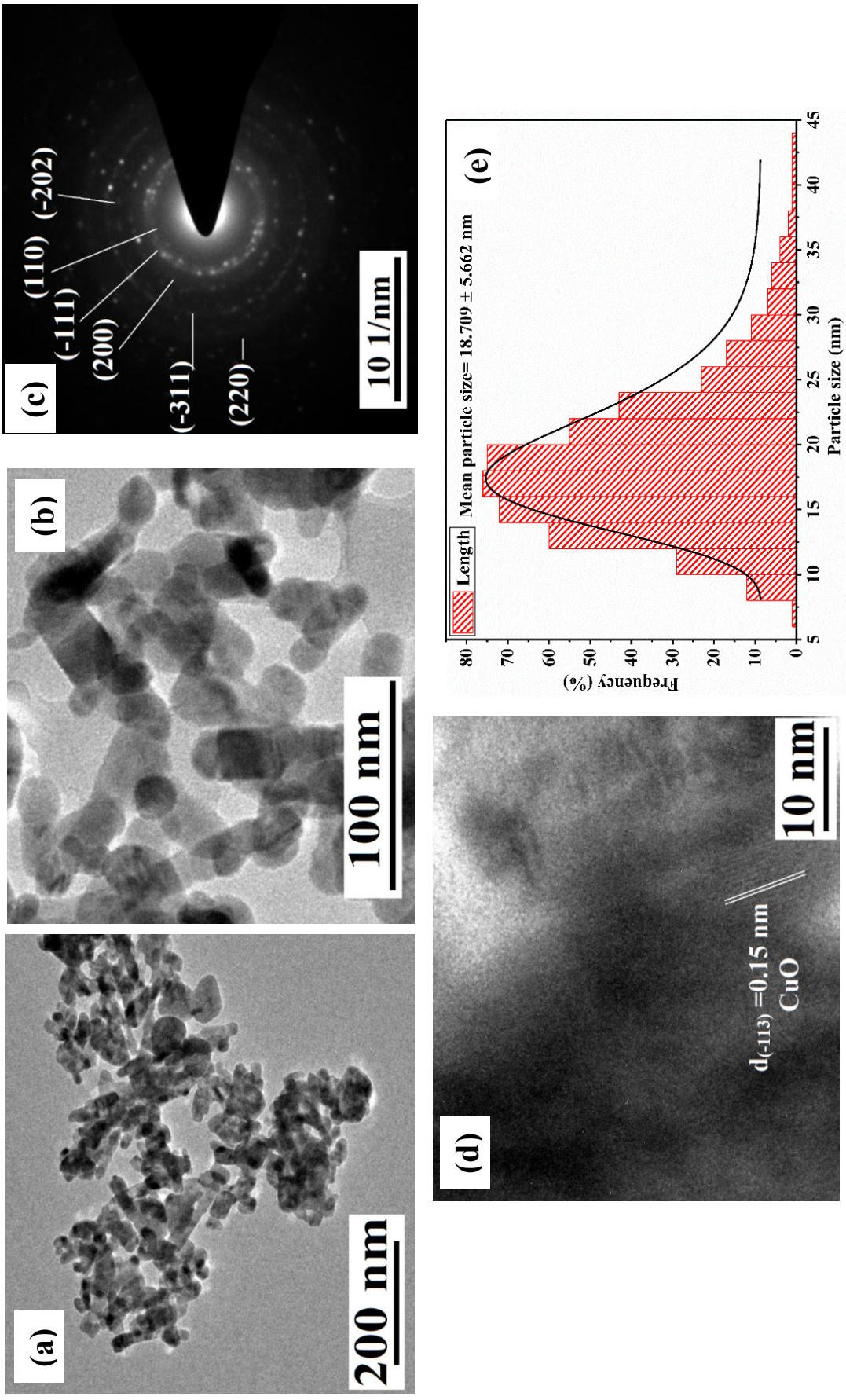

Figure 4.5 TEM images at various magnifications (a,b), SAED pattern (c), High resolution-TEM image with interplanar d-spacing (d), particle size distribution plot (e) of as-synthesized N1 nanoparticles

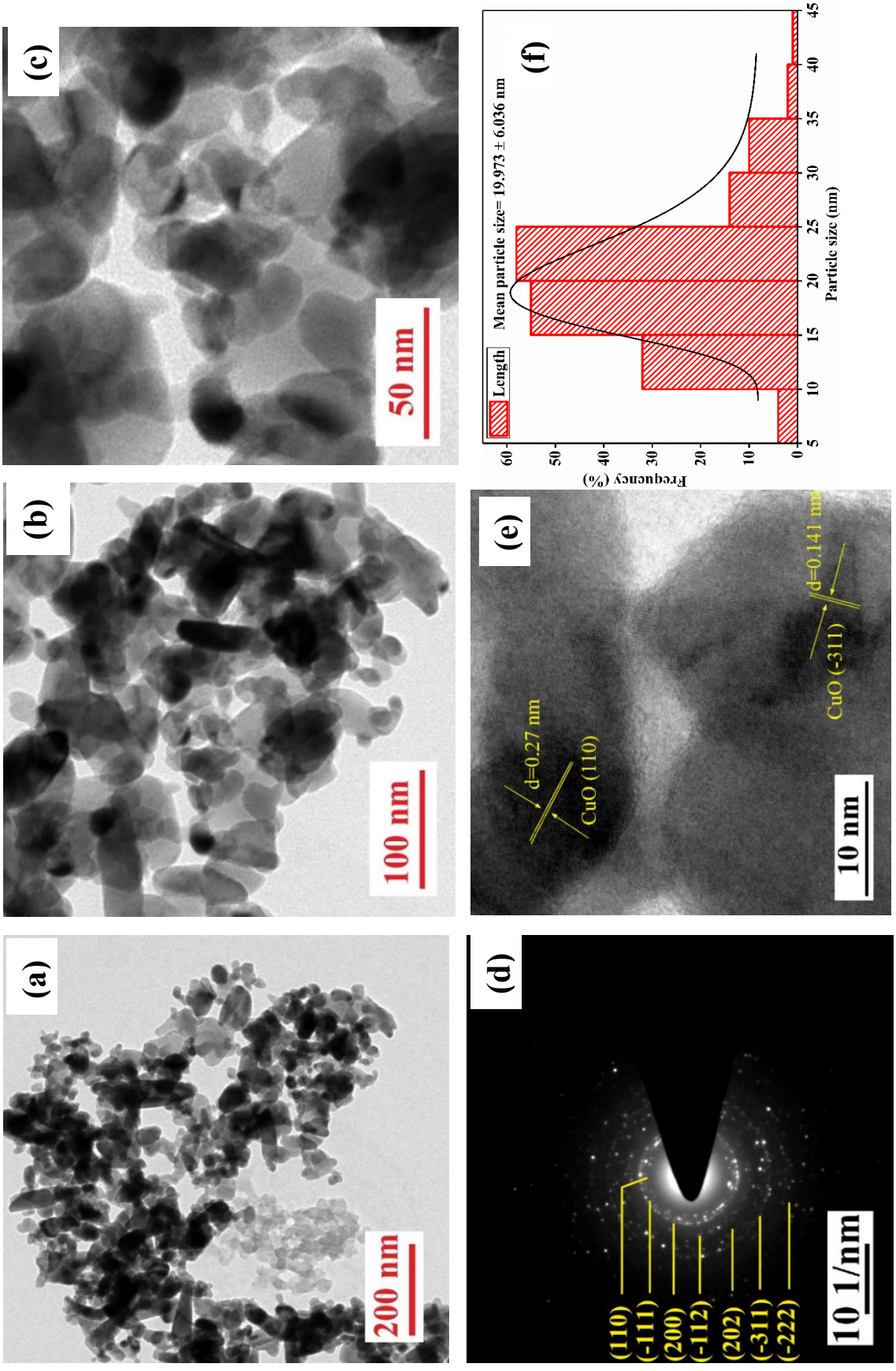

Figure 4.6 TEM images at various magnifications (a–c), SAED pattern (d), High resolution-TEM image with interplanar d-spacing (e), particle size distribution plot (f) of as-synthesized N2 nanoparticles

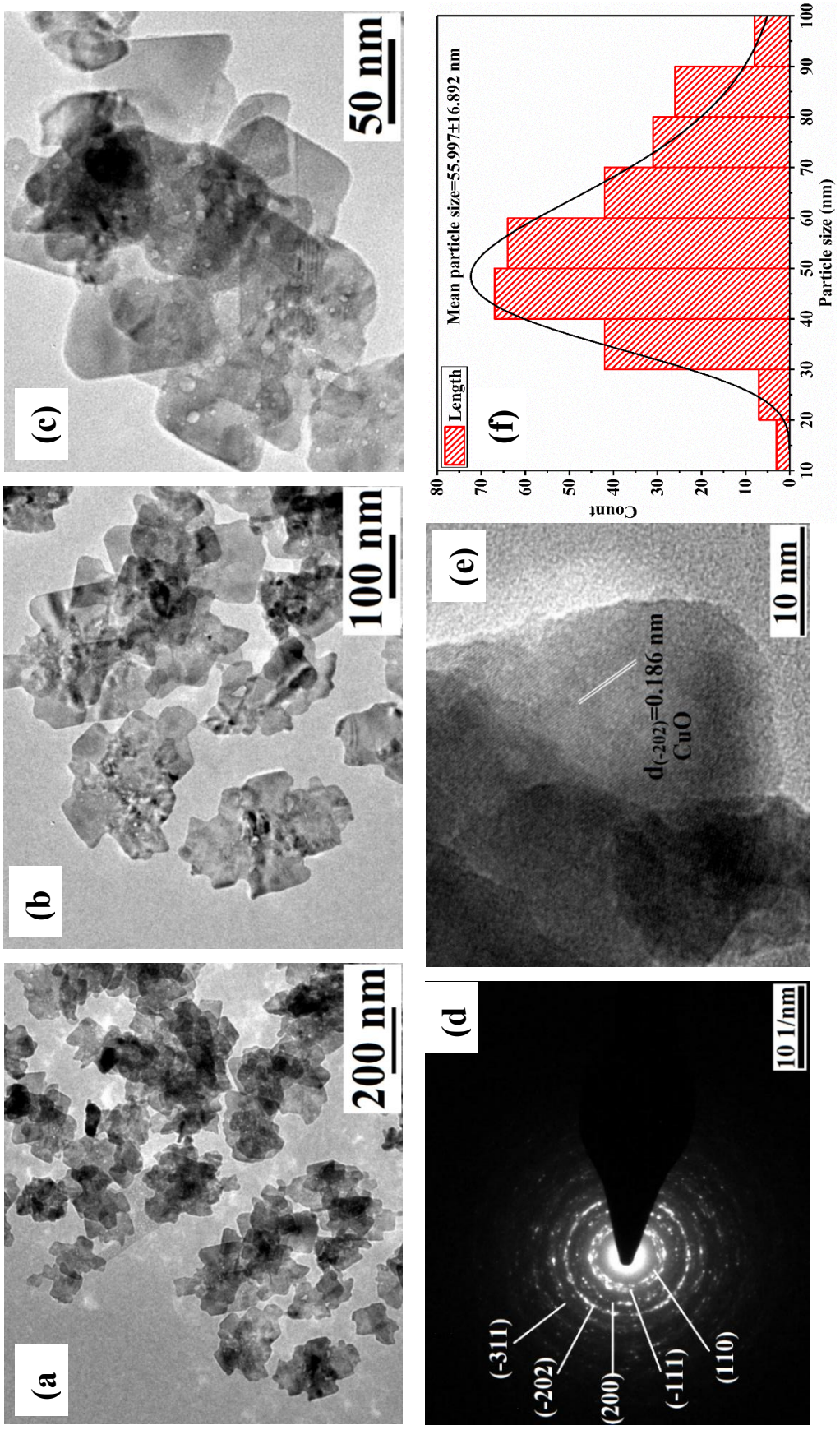

Figure 4.7 TEM images at various magnifications (a–c), SAED pattern (d), High resolution-TEM image with interplanar d-spacing (e), particle size distribution plot (f) of as-synthesized N3 nanoparticles

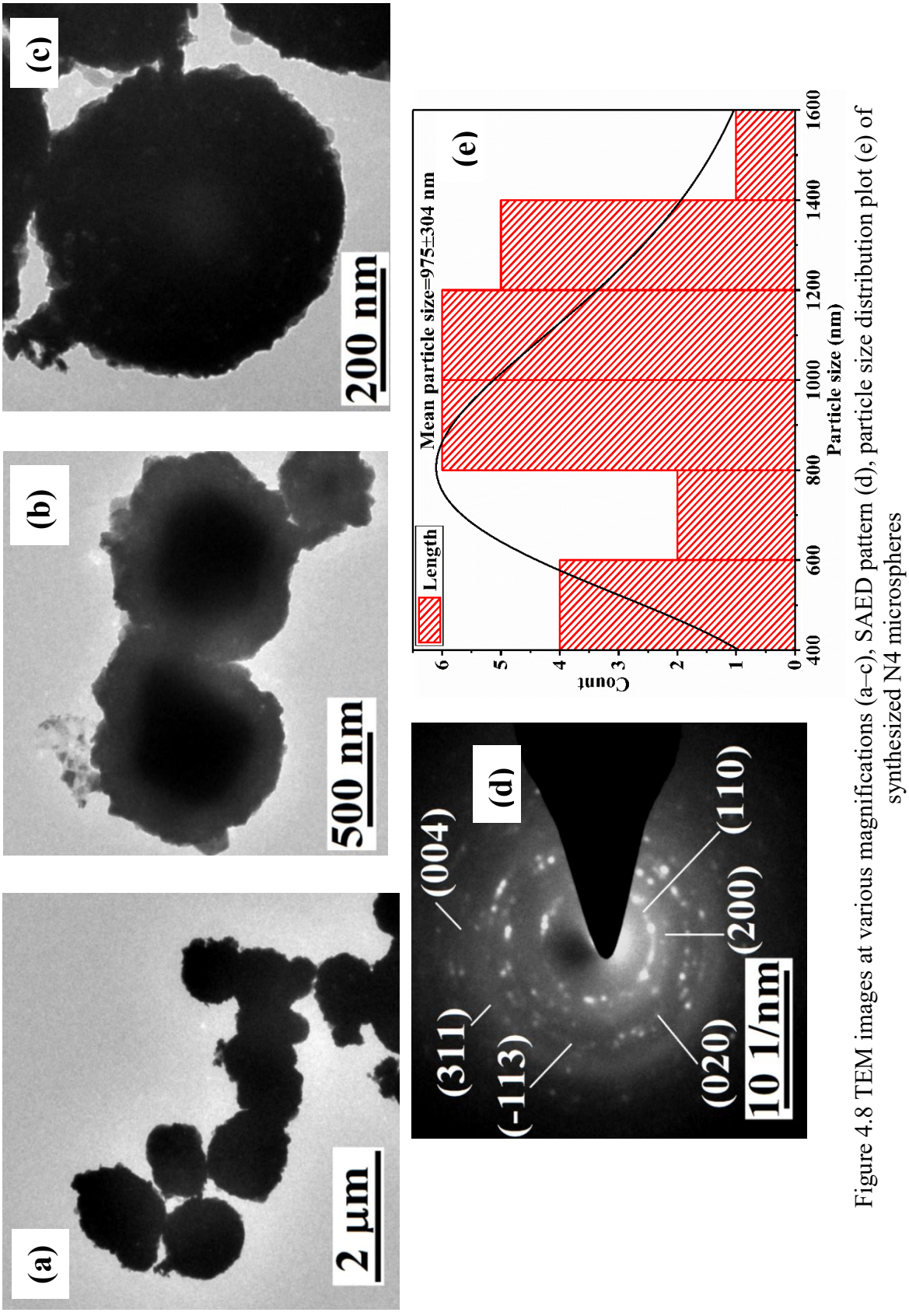

Figure 4.8 TEM images at various magnifications (a–c), SAED pattern (d), particle size distribution plot (e) of synthesized N4 microspheres

4.3.4. XPS analysis

XPS analysis is a method highly sensitive to surface properties, utilized for validating the elemental makeup, purity, and oxidation state of CuO NPs. XPS analysis of sample N1 and N2 is performed. The XPS survey spectrum (*Figure 4.9*) indicates the existence of Cu, O, and C in sample N1, and the presence of Cu, O, C, and Zn in sample N2. N2 contains 1.69 atomic % Zn, which is a very small fraction, so it was not seen in HR-XRD results of N2 (*Figure 4.1*). The deconvolution of all spectra was conducted using Casa XPS software, using the carbon signal at 282.8 eV as the reference point.

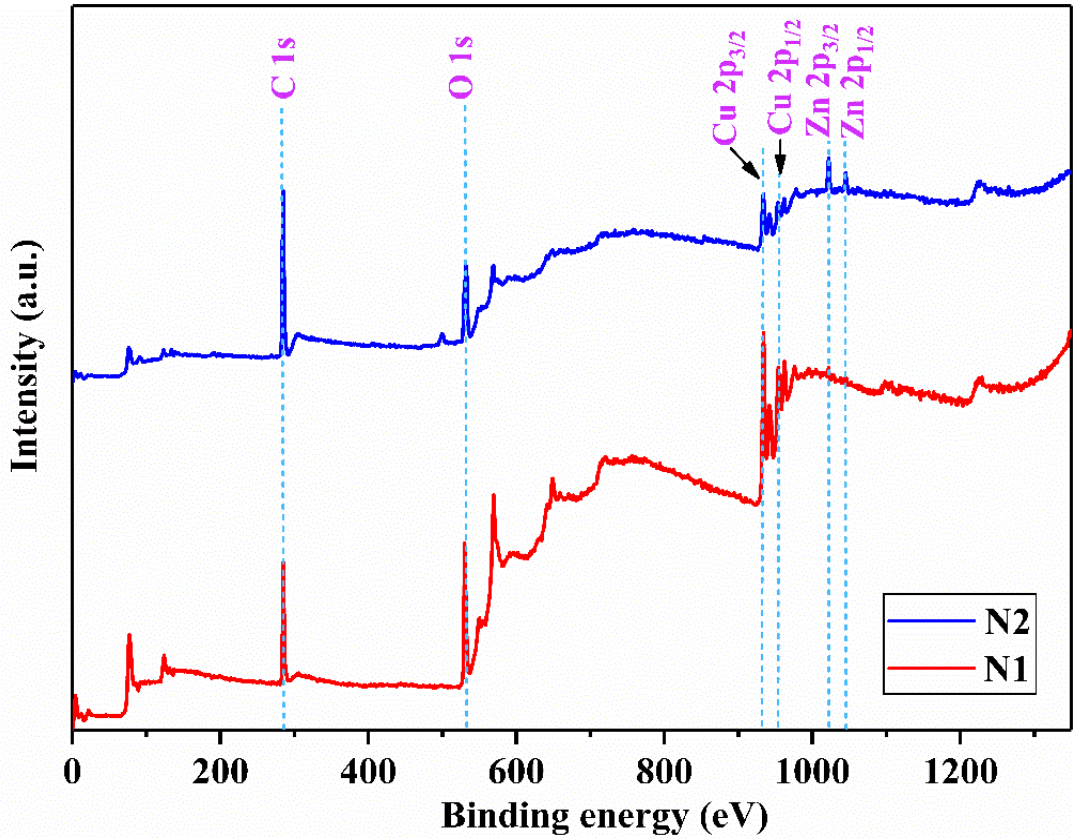

Figure 4.9 XPS widescan spectra of N1 and N2 sample

In the case of the N1 sample, the high-resolution XPS spectrum of Cu 2p (*Figure 4.10(a)*) reveals two wide peaks positioned approximately at 933.5 and 953 eV, corresponding to the Cu $2p_{3/2}$ and Cu $2p_{1/2}$ positions, respectively. These peaks are indicative of Cu ions

bound to oxygen ions. The existence of two satellite peaks, situated approximately 10 eV higher than the Cu $2p_{3/2}$ and Cu $2p_{1/2}$ peaks, is linked to the partially filled d-block ($3d^9$) of Cu^{2+}. This observation serves as confirmation for the formation of CuO and rules out the possibility of the existence of a Cu_2O phase (Ethiraj and Kang, 2012). Moreover, the spacing between Cu $2p_{3/2}$ and Cu $2p_{1/2}$ is approximately 20.01 eV, consistent with the standard spectrum of Cu (Akhavan et al., 2011; Ethiraj and Kang, 2012). The lower energy peak at 529.5 eV (*Figure 4.10(b)*) arises from oxygen within the CuO crystal lattice, aligning with the characteristic energy for O^{2-} in CuO, specifically the oxygen-copper bonds (O-Cu) (Xu et al., 1999). The peak at 531.3 eV (in *Figure 4.10(b)*) may be attributed to the binding energy of oxygen defects or vacancies present within the CuO matrix (Khan et al., 2020). The peaks at higher energy around 533 eV are linked to chemisorbed oxygen, specifically oxygen adsorbed onto the surface of N1, likely in the form of water adsorbed on the surface (Ibupoto et al., 2013; Zarate et al., 2007).

Similar observations arise from the HR-XPS analysis of Cu and O in the N2 sample (*Figure 4.11(a,b)*). Alongside Cu and O, the presence of Zn is evident in N2 (*Figure 4.9*). The binding energies of Zn 2p (in *Figure 4.11(c)*) at 1022.1 and 1045.2 eV, attributed to Zn $2p_{3/2}$ and Zn $2p_{1/2}$ respectively, signify Zn^{2+} occupying the regular lattice site of ZnO (Sahai and Goswami, 2014). Notably, the binding energy difference of 23.104 eV between Zn $2p_{3/2}$ and Zn $2p_{1/2}$ emissions aligns with the characteristic value for ZnO (Pandey et al., 2013; Sahai and Goswami, 2014). The XPS analysis of O 1s in both N1 and N2 indicates a higher atomic percentage of oxygen vacancies in N1 compared to N2 (*Table 4.3*).

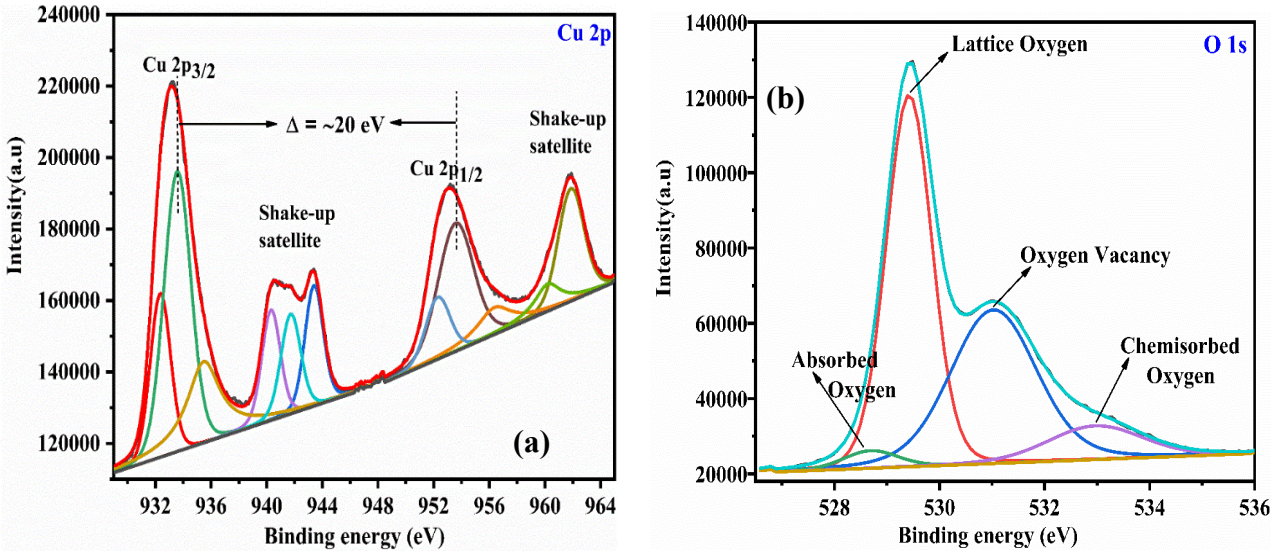

Figure 4.10 Deconvoluted XPS spectra of Cu 2p (a) and O 1s (b) for the as-prepared N1

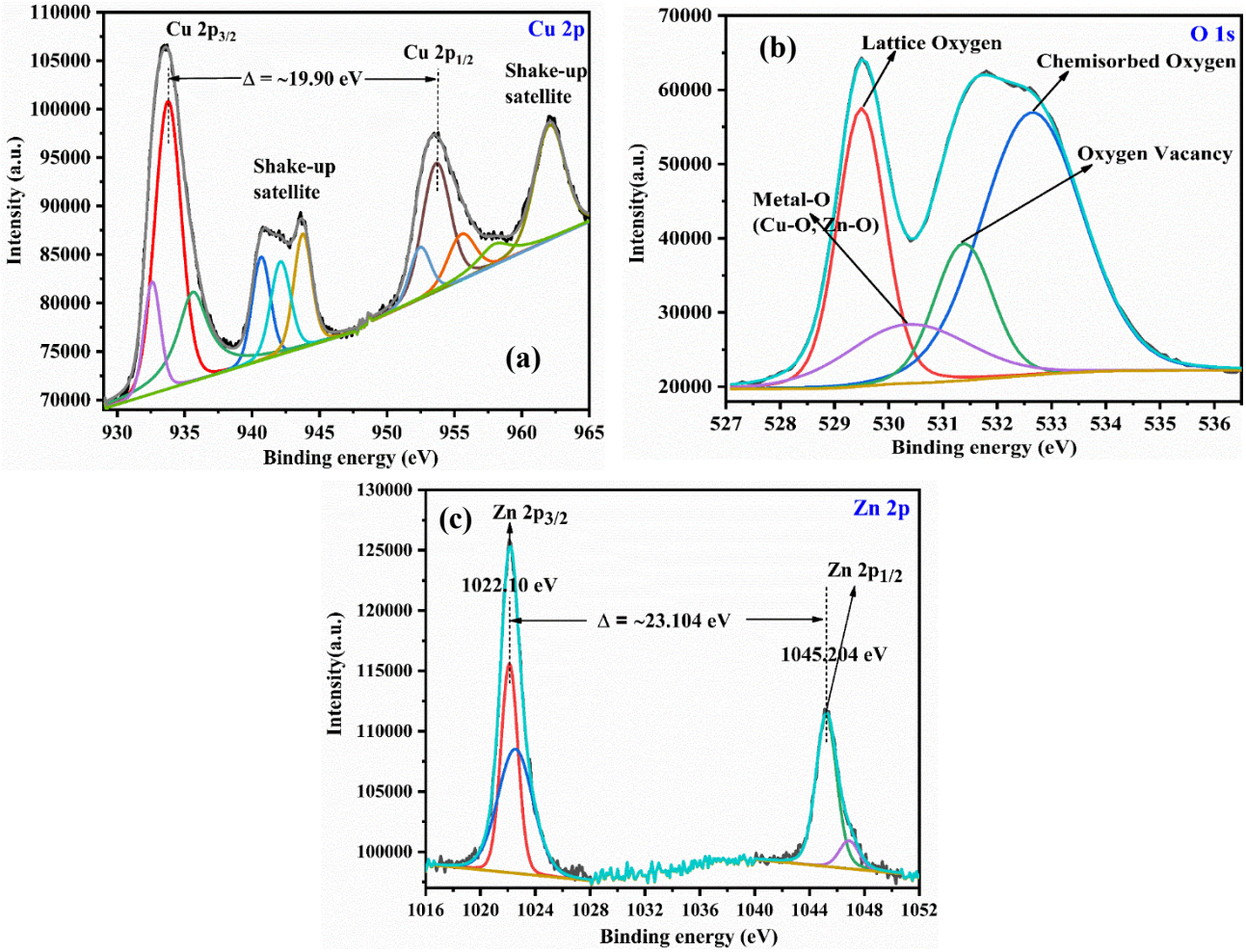

Figure 4.11 Deconvoluted XPS spectra of Cu 2p (a), O 1s (b) and Zn 2p (c) for the as-prepared N2 sample

Table 4.3 Atomic weight% of elements present in N1 and N2

Sample name	Atomic %		
	$O_{lattice}$	$O_{vacancy}$	$O_{chemisorbed}$
N1	52.34	39.88	7.78
N2	29.45	31.34	39.21

4.3.5. Surface area measurements

The absorption and desorption isotherm of N1 (*Figure 4.12(a)*) and N2 (*Figure 4.12(c)*) exhibit Type IV isotherm, revealing mesoporous characteristics of the product. IUPAC proposed to define nanopores by their internal pore width which is the diameter in case of cylindrical pore. According to IUPAC classification, a material is termed mesoporous if its pore size is between 2-50 nm (Alothman, 2012; Donohue and Aranovich, 1998; Sing et al., 1985). From BET method, the specific surface area was found to be 32.4 m^2/g and 28 m^2/g for N1 and N2 samples respectively. The mean pore diameter of the as-recovered nanoproduct was determined to be 15.549 and 18.051 nm for N1 and N2 respectively, which is in the mesoporous region. The pore volume was ascertained to be 0.1201 and 0.1018 cm^3/g for N1 and N2 respectively. The BJH pore size distribution plot in *Figure 4.12(b,d)* indicates that maximum of the pore size distribution in sample N1 and N2 is mainly concentrated between 2-20 nm, which is the mesoporous region (Lowell et al., 2004), and few macropores (size >50 nm) were also present. Micropores have pores of internal width less than 2 nm. The pore size distribution curve maximum is pointed at 2.461 nm. Differential pore volume, sometimes called as differential pore volume distribution means pore size distribution, or porosity spectrum. It gives a spectrum of porosity based on

the relative abundance of voids on the micro-, meso-, and macropore range. It is a more valuable metric than total porosity as it can provide detailed insights into more complex properties such as localized density. This can be extremely useful in defect analysis, and quality assurance where powder uniformity is a critical parameter.

Large BET surface area of the nanoparticles contribute to the increase of surface oxygen vacancies, which improve visible light absorption and act as active sites for photocatalytic reactions leading to enhancement of photocatalytic activity of CuO NPs under visible light irradiation (Jing Wang et al., 2016). This can be used for pollutant degradation studies in wastewater treatment to combat water pollution (Tammina et al., 2018).

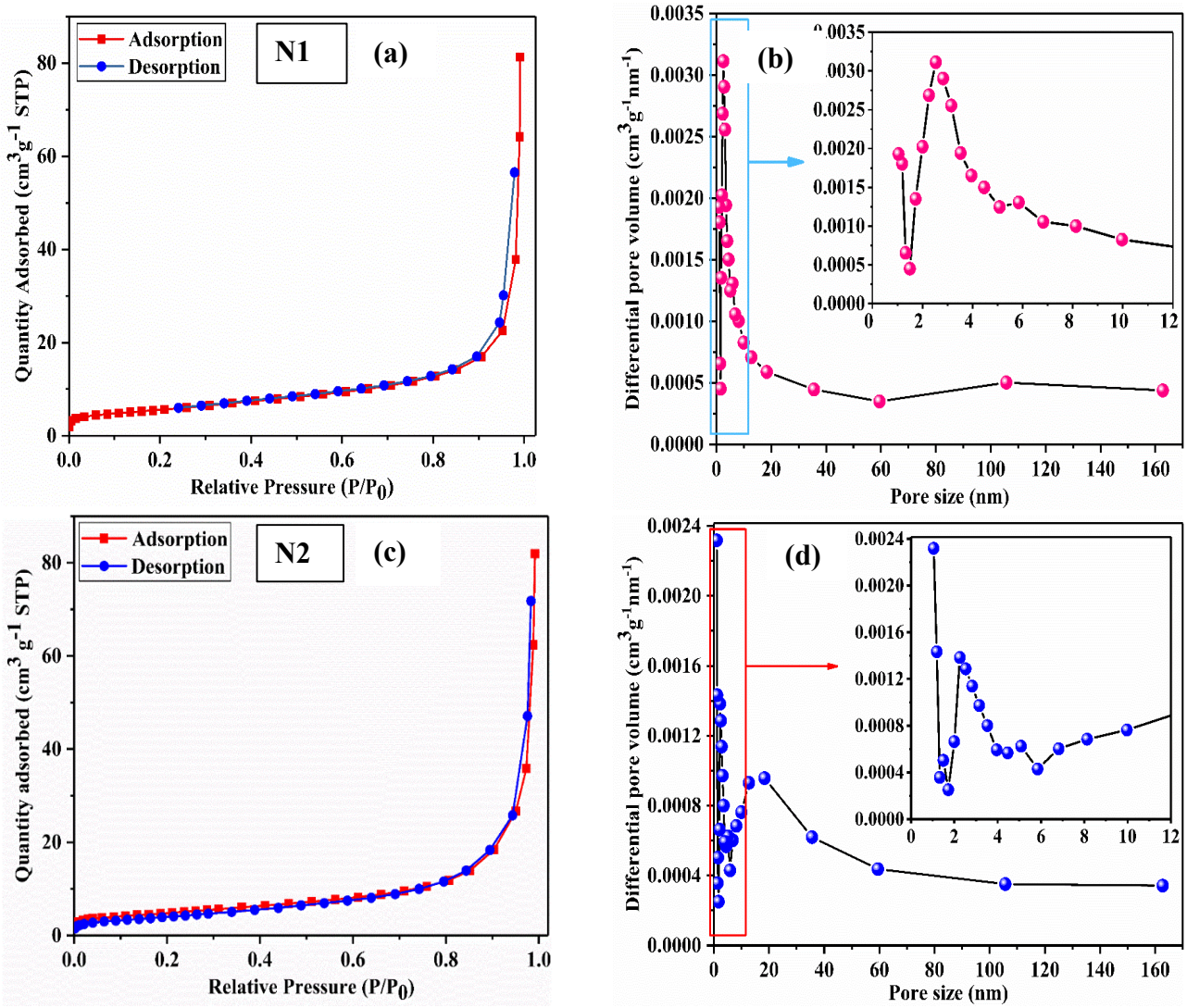

Figure 4.12 (a, c) N_2 adsorption−desorption isotherm and (b, d) corresponding BJH pore size distribution curve of N1 and N2

4.4. Conclusions

- This study explained a scheme to recover copper as copper oxide from waste PCBs of computer motherboards.
- HR-XRD showed that precipitation of leached solution with sodium hydroxide lead to formation of monoclinic copper oxide after calcination (as in case of N1 and N2 samples), whereas precipitation with 2 M NaOH solution and 2 M aqueous

ammonia solution accompanied by 60°C working temperature lead to formation of CuO/ZnO phase.

- EDX attached to SEM confirmed the presence of copper and oxygen confirming the formation of CuO in N1, N2, and N3 samples, whereas peaks of copper, zinc and oxygen were observed in the EDS of N4 sample which confirmed the formation of CuO/ZnO structure.
- TEM showed that synthesized nanostructures N1 and N2 are made of irregular spherical morphology, whereas N3 is made of sheet type morphology. N4 sample is made of larger microspheres type morphology. The average particle size of N1, N2, N3 and N4 product is found to be 18.709±5.662 nm, 19.973±6.036 nm, 55.997±16.892 nm, and 975±304 nm respectively from the particle size distribution plot.
- From the Tauc plot, the bandgap energy of N1, N2, N3 and N4 samples was found to be 1.93, 1.97, 1.86 and 1.48 eV.
- A higher atomic percentage of oxygen vacancies is observed in N1 compared to N2 from the XPS analysis of O 1s of N1 and N2 samples.
- The N2 adsorption/desorption isotherm of N1 and N2 exhibits Type IV isotherm, revealing mesoporous characteristics of the sample. From BET method, the specific surface area of N1 and N2 sample was found to be 32.4 and 28 m^2/g respectively. The BJH pore size distribution plot indicates that maximum of the pore size distribution is mainly concentrated between 2 and 20 nm, which is the mesoporous region, and few macropores (size >50 nm) were also present.